frontiers | Frontiers in Earth Science

TYPE Original Research
PUBLISHED 18 March 2025
DOI 10.3389/feart.2025.1569706

Check for updates

OPEN ACCESS

EDITED BY
Xin Sun,
Sinopec Matrix Co., LTD., China

REVIEWED BY
Xin Nie,
Yangtze University, China
Peng Zhu,
Chengdu University of Technology, China

*CORRESPONDENCE
XueFeng Liu,
liuxf@upc.edu.cn

RECEIVED 01 February 2025
ACCEPTED 03 March 2025
PUBLISHED 18 March 2025

CITATION
Xian F, Chen M, Li M, Dai Q, Xia F, Lee Z, Hou J and Liu X (2025) Experimental study of electrical resistivity in tetrahydrofuran hydrate-bearing sediments.
Front. Earth Sci. 13:1569706.
doi: 10.3389/feart.2025.1569706

COPYRIGHT
© 2025 Xian, Chen, Li, Dai, Xia, Lee, Hou and Liu. This is an open-access article distributed under the terms of the Creative Commons Attribution License (CC BY). The use, distribution or reproduction in other forums is permitted, provided the original author(s) and the copyright owner(s) are credited and that the original publication in this journal is cited, in accordance with accepted academic practice. No use, distribution or reproduction is permitted which does not comply with these terms.

Experimental study of electrical resistivity in tetrahydrofuran hydrate-bearing sediments

Fei Xian[1], Ming Chen[2], Min Li[1], Qin Dai[1], Fujun Xia[1], Zizeng Lee[1], Jian Hou[3] and XueFeng Liu[1]*

[1]College of Science, China University of Petroleum (East China), Qingdao, China, [2]CNOOC(China) Co, Ltd., Zhanjiang, Guangdong, China, [3]School of Petroleum Engineering, China University of Petroleum (East China), Qingdao, China

Natural gas hydrates, solid crystalline structures formed by the combination of natural gas and water molecules under high-pressure and low-temperature conditions, are regarded as a promising clean energy source. Electrical resistivity serves as a fundamental petrophysical parameter for quantifying natural gas hydrate saturation in sand-dominated sediments, with its sensitivity to pore-filling hydrate morphology and distribution patterns. An integrated experimental system combining *in-situ* CT scanning and resistivity measurement was developed to investigate tetrahydrofuran (THF) hydrate formation dynamics in quartz sand sediments. We prepared four distinct THF solutions to represent different hydrate formation regimes, lowered the temperature within a reactor containing quartz grains, and continuously monitored the electrical resistivity of the sediments during the hydrate formation. Additionally, CT scanning was used to acquire three-dimensional grayscale images at varying hydrate saturation. The experimental resistivity data revealed pronounced deviations from classical Archie's equation, demonstrating complex behavior between the resistivity index and water saturation. The CT scan images demonstrate a pronounced salting-out effect during the hydrate formation process. The precipitation of dissolved salts significantly increased the salinity of formation water, resulting in a corresponding decrease in resistivity due to enhanced ionic conductivity. The phenomenon significantly impedes hydrate formation kinetics, causing a substantial divergence between the measured hydrate saturation and the thermodynamic equilibrium prediction. When temperature effects and salt precipitation phenomena are properly accounted for, the resistivity index-water saturation relationship exhibits excellent agreement with Archie's law, enabling reliable estimation of hydrate saturation in quartz-dominated sediments.

KEYWORDS

tetrahydrofuran hydrate, electrical resistivity, sand sediments, salting-out effect, non-archie behavior

1 Introduction

Natural gas hydrates produce almost no residual waste after combustion and result in minimal pollution, making them a clean and viable alternative to oil as an energy source (Zhou et al., 2019). Sufficient reserves of natural gas hydrates hold vast energy potential and economic value (Chong et al., 2016; Yu et al., 2021). As gas hydrate drilling technology advances (Wei et al., 2022), successful global test mining offers hope for the development

of this potential new energy source. Natural gas hydrates form under low-temperature and high-pressure conditions (Wilcox et al., 1941). They exhibit an ice-like crystalline solid structure characterized by a cage-like framework composed of water molecules that encapsulate guest molecules. Most natural gas hydrates are primarily distributed in deep-sea regions, with only approximately 3% located in permafrost layers on land. The technology for extracting and developing combustible ice both domestically and internationally is still in its early stages (Tan et al., 2016; Du et al., 2024). There is an urgent need to advance research on extraction methodologies, formation mechanisms, and material properties, (Lijith et al., 2019), a while critical technological challenges remain at a pivotal stage requiring focused breakthroughs (Konno et al., 2016). However, the extraction and utilization of natural gas hydrates face significant technical and economic challenges, necessitating in-depth research into their physical properties and behavior under various conditions.

Hydrate reservoirs display distinct characteristics such as high resistivity, rapid sonic propagation speeds, and elevated capillary pore pressures (Guerin et al., 1999; Collett and Lee, 2012; Sahu et al., 2020). The electrical properties of hydrate reservoirs serve as a foundation for evaluating porosity and hydrate saturation (Xing et al., 2022). Spangenberg investigated the electrical properties of glass bead sediments in relation to methane hydrate saturation, establishing a logarithmic relationship between resistivity indices and water saturation (Spangenberg and Kulenkampff, 2006). Chen designed and developed a CT-based resistivity measurement system for hydrate-containing sediments, which included the gas hydrate experimental simulation part, the resistivity measurement part and the CT scan part (Chen et al., 2018). The resistivity and CT images during hydrate formation *in situ* were simultaneous monitored. However, the influence of hydrate micro-distribution on resistivity has not been thoroughly investigated to provide supportive data. This oversight has led to the revelation of significant non-uniformities in conductivity shifts across various regions, which are indicative of non-homogeneous hydrate formation. The spatial heterogeneity of methane hydrate distribution results in significant discrepancies between calculated and actual reservoir saturation levels. To address this challenge and achieve reliable gas hydrate saturation estimates, they proposed a dual-parameter computational model that integrates resistivity and acoustic time difference measurements derived from logging data (Li H. et al., 2022).

The formation of methane hydrates requires high-pressure, low-temperature conditions, necessitating specialized high-pressure equipment for experimental studies. This makes experiments with methane hydrates more challenging and expensive (Hirai et al., 2001; Hassanpouryouzband et al., 2020). Tetrahydrofuran (THF) can form Type II hydrates with water at atmospheric pressure and temperatures of 4°C or lower (Lee et al., 2007; Li et al., 2019), which facilitates experimental manipulation and control. Besides, THF hydrates have similar physical properties to methane hydrates in terms of mechanical, acoustic, and electrical characteristics (Nagashima et al., 2005; Spangenberg and Kulenkampff, 2006; Yun et al., 2007; Fang et al., 2017). THF molecules are completely miscible with water, allowing for precise control over the hydrate volume fraction. Although there are differences in formation conditions and decomposition, THF hydrates are frequently used as a substitute for methane hydrates in laboratory experiments.

The Archie equation establishes a quantitative relationship between reservoir hydrocarbon saturation and resistivity logging data. According to Archie's equation, in a log-log coordinate system, the resistivity index and water saturation are linearly related. Research on the electrical properties of THF hydrates has shown that calculating hydrate saturation using electrical models requires consideration of multiple factors. During hydrate formation, the resistivity index (*RI*) and water saturation (S_w) do not follow a linear relationship in the log-log coordinate system, a phenomenon known as the "non-Archie effect" (Shankar and Riedel, 2011; Zhang et al., 2021). Under such circumstances, applying the Archie equation to calculate hydrate saturation from resistivity may result in significant errors. Li et al. investigated the resistivity variations of THF hydrates in different soil types with varying hydrate saturations, revealing that the resistivity of THF hydrate-bearing soils correlates with their SiO_2 content; higher hydrate saturation leads to lower resistivity. However, due to limitations in the precision of the constant-temperature system, the resistivity change curve for THF hydrates with different saturation levels was not obtained (Li et al., 2020). The resistivity of hydrate spikes during formation, and the presence of saline water in hydrates reduces resistivity (Shankar and Riedel, 2011). The evolution of resistivity process in different systems are different, and the salting-out effect reduces sediment resistivity during the nucleation phase (Chen et al., 2022). Electrical resistivity was measured on samples of Berea Sandstone and Austin Chalk that were saturated with a stoichiometric mixture of THF and water. The electrical resistivity increased nearly 2 orders of magnitude upon hydrate formation and continued to increase slowly as the temperature was decreased. Resistivities were strongly a function of the dissolved salt content of the pore water (Pearson et al., 1986).It is evident that hydrate reservoir resistivity is closely related to factors such as temperature, hydrate saturation, and the salting-out effect (Ren et al., 2010; Wang et al., 2011; Li et al., 2012; Dong et al., 2019). However, there are still challenges in THF hydrate electrical experiments regarding formation water salinity, temperature, and saturation calculations.

To address these challenges, this study will conduct rock electrical experiments using THF hydrates. By analyzing the salting-out effect during hydrate formation and its relationship with formation water salinity and resistivity, the study will identify deviations between theoretical and measured hydrate saturations. After corrections for temperature, salinity, and saturation, the calculated hydrate saturation in sediments and increased resistivity can be used to determine parameters for the saturation evaluation model. This model will facilitate hydrate saturation, laying the groundwork for subsequent research on weakly cemented natural gas hydrates in the South China Sea.

2 Experimental method

2.1 Experimental device

The *in-situ* CT scanning and resistivity measurement device for hydrate-bearing sediments primarily consists of a THF hydrate reactor, a low-temperature chamber, an electrical measurement system, and a CT scanning device, as shown in Figure 1. To ensure the penetration of X-rays, the THF hydrate reactor is

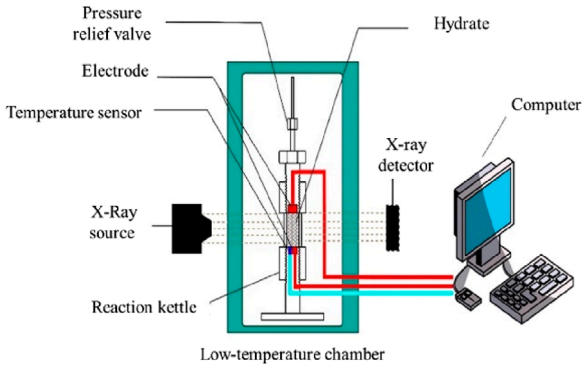

FIGURE 1
Schematic diagram of the X-CT experimental setup.

fabricated from PEEK. Given the trade-off between CT scanning resolution and sample size, the sample chamber diameter is designed to be 10 mm, ensuring sufficiently high resolution. Quartz grains can be placed inside the sample chamber to form a quartz sediment model. Compared to the formation conditions of methane hydrates, the formation of THF hydrates requires only a low-temperature environment. This apparatus uses forced-air cooling to lower the temperature inside the insulated chamber to meet the temperature requirements for THF hydrate formation. The resistivity measurement is conducted using a two-electrode method, with electrodes connected to a digital bridge that measures resistance across the reactor in real-time and converts it to electrical resistivity. The CT scanner used in this study is the nano Voxel 3,000 micro-CT scanner from Sanying Precision Company The reactor, low-temperature chamber, and measurement electrodes are placed inside the X-ray CT scanner and connected to external control devices *via* pipelines and cables. The hydrate formation experiments are conducted entirely within the CT scanner to ensure that the scanned region remains consistent throughout different stages of hydrate formation, thereby providing a basis for analyzing the spatial distribution of hydrates.

2.2 Experimental sample

For weakly cemented and compacted pure sandstone, the size of the pore space is directly proportional to the grain size of quartz particles. Differences in sediment type, pore structure, and pore water salinity can influence the relationship between pore fluid resistivity and hydrate saturation in experiments (Jin et al., 2020). To achieve higher accuracy in pore space identification from CT images, natural sea sand with a mesh size of 20–40 (grain diameter of 0.425–0.85 mm) is employed as a sediment analog. The saturation of THF hydrates in mixtures with water depends on the mass ratio of the two substances, meaning that the saturation can be controlled by adjusting the ratio of pure tetrahydrofuran to deionized water. The amount of the substance n_{THF} after the complete formation of the hydrate can be expressed Equation 1.

$$n_{\mathrm{THF}} = \frac{\rho_{\mathrm{THF}} V_{\mathrm{THF}}}{M_{\mathrm{THF}}} \tag{1}$$

where, V_{THF} and M_{THF} represent the volume and mass of THF, respectively, and ρ_{THF} is the density of THF, which is taken as a constant value 0.89 g/cm^3. The molecular formula of THF hydrate is $CH_4H_8O{\cdot}17H_2O$. The formation of THF hydrate requires 17 times as many H_2O molecules as THF molecules. Therefore, the residual water volume $V_{residual-H_2O}$ can be expressed by Equation 2.

$$V_{residual-H_2O} = \left(\frac{\rho_w V_w}{M_w} - 17 \times \frac{\rho_{\mathrm{THF}} V_{\mathrm{THF}}}{M_{\mathrm{THF}}} \right) \times \frac{M_w}{\rho_w} \tag{2}$$

where the ρ_w, V_w and M_w represent the density, volume and mass of the solution, respectively. And the saturation of the residual water can be expressed as:

$$S_w = \frac{V_{residual-H_2O}}{V_{\mathrm{THF}} + V_w} \tag{3}$$

So the THF hydrate saturation S_h is calculated.

$$S_h = \frac{4.7673 M_{\mathrm{THF}}}{M_w \rho_{\mathrm{THF}} + M_{\mathrm{THF}}} \times 100\% \tag{4}$$

According to Equation 4, the hydrate saturations in the sediment pores, following the complete formation of THF hydrates from solutions with weight fractions of 6.35%, 8.33%, 12.12%, and 19.05%, are 30%, 40%, 60%, and 100%, respectively.

CT scanning can be used to obtain three-dimensional grayscale images of the sediments. The grayscale values in the images depend on the density of the components at the corresponding positions, and thus can be used to distinguish between the rock matrix and pore fluids. After hydrate formation, the pores contain two components: THF hydrate and formation water. Since the densities of the hydrate and formation water are similar, they are difficult to distinguish in the grayscale images obtained by CT scanning. To enhance the contrast between the hydrate and formation water, this study uses a sodium iodide (NaI) solution instead of a sodium chloride (NaCl) solution. The presence of iodide ions in the NaI solution significantly increases the X-ray absorption coefficient, resulting in a marked increase in the brightness of the grayscale images in regions where the NaI solution occupies the pores. Previous studies have shown that under low-concentration conditions, the effects of halide ions on hydrate phase equilibrium are approximately comparable (Yang et al., 2012; Asadi et al., 2019). Therefore, in this study, a 5% NaI solution is added to the THF solution to match the salinity of seawater.

2.3 Resistivity measurement

Initially, sand grains with 20–40 mesh was packed into the reactor. Subsequently, the sediment pores were saturated with the prepared THF solution. The reactor was then placed into the low-temperature chamber, which was placed on the sample stage of the CT scanner. Finally, the low-temperature chamber lines, resistivity and temperature measurement circuits were connected. In the experiment, a low-temperature chamber and a digital bridge measurement system were utilized to monitor real-time changes in pore fluid resistivity as a function of temperature. By gradually lowering the reactor temperature and recording resistivity at various points, we quantitatively analyzed the temperature effect on the

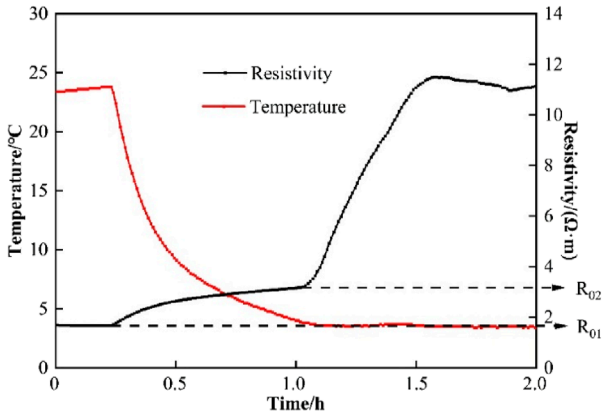

FIGURE 2
Variation curves of resistivity and temperature during the formation of THF hydrate solution.

resistivity at both ends of the sediment. As hydrate formation is an exothermic process, the increase in the temperature curve indicates the initiation of hydrate formation.

The changes in temperature within the reactor and the electrical resistivity of the sediments over time during the formation of THF hydrates are shown in Figure 2, with the results corresponding to a THF mass fraction of 19.05%. The results indicate that as the temperature inside the reactor decreases, the electrical resistivity gradually increases. When the temperature drops to around 3°C, the resistivity tends to stabilize. A slight temperature rebound indicates that an exothermic reaction occurring within the reactor, accompanied by an increase in resistivity, which signifies the initiation of hydrate formation. Once the hydrate is fully formed, the electrical resistivity gradually approaches a stable value, representing the resistivity of the sediments at the corresponding hydrate saturation level. In Figure 2, R_{01} represents the resistivity of the fully water-saturated sediments at room temperature before the temperature decrease, while R_{02} denotes the resistivity of the fully water-saturated sediments before hydrate formation at a lowered temperature.

2.4 *In-situ* CT scanning and image processing

X-ray CT, known as X-ray computed tomography, is an advanced X-ray imaging technique that uses a computer to reconstruct cross-sectional images from X-ray tomographic scans, enabling non-destructive detection of the composition and structure of opaque objects (Kalender, 2006). After the THF solution in the sediment pores has fully converted into hydrates, X-ray CT scanning can be employed to generate three-dimensional grayscale images of the sediments, as shown in Figure 3a. The scanning parameters are: voltage 80.0 kV, current 180.0 μA, exposure time 0.82 s, number of image averages 2, and resolution 8.1 μm. In this study, X-CT scanning was performed *in situ*. The resolution of X-CT scans is at the micrometer level, and even slight vibrations can cause shifts in the obtained X-CT images. To ensure the accuracy of image processing and analysis, image registration algorithms were used to correct image shifts after acquiring X-CT images at different time points, ensuring the accuracy of the data (Li B. et al., 2022; Li et al., 2023).

Figure 3b shows a two-dimensional grayscale cross-section of the hydrate-bearing sediments, with varying grayscale values represent different components. Due to the replacement of NaCl with NaI, the NaI solution exhibits higher brightness, while the slightly dimmer regions correspond to quartz grains. The presence of minor high-density minerals in the natural sea sand is manifested as bright spots in the grayscale image. The darkest areas in the image represent hydrates and bubbles, with bubbles resulting from incomplete saturation of the sediments. As bubbles exhibit lower brightness than hydrates, they can be distinguished from hydrates by their grayscale values.

By applying filtering, noise reduction, registration and threshold segmentation to the scanned grayscale images, the bubbles, hydrates, aqueous solutions, and quartz grains in the sediments after hydrate formation can be distinguished. The number of pixels occupied by each component in the image is then counted. The hydrate saturation is calculated by dividing the number of hydrate pixels by the total number of pore pixels (including those for hydrates, formation water, and bubbles).

3 Experimental results resistivity measurement results

3.1 Resistivity measurement result

The resistivity of the sediments after complete hydrate formation was recorded. The formation factor F and the resistivity increase ratio RI can be calculated using Equations 5, 6:

$$F = \frac{R_0}{R_w} = \frac{a}{\phi^m} \tag{5}$$

$$RI = \frac{R_t}{R_0} = \frac{b}{S_w{}^n} \tag{6}$$

where R_0 and R_w are the resistivities of the rock saturated with formation water and the formation water itself, respectively, in units of $\Omega \cdot m$; a and b are lithological coefficients; m and n are the cementation and saturation exponents, respectively; ϕ is the rock porosity; and S_w is the water saturation.

The hydrate saturation was calculated based on the THF solution concentration, allowing for the determination of the water saturation S_w under different concentration conditions. Compared to conventional oil and gas reservoir rock-electric experiments, in the rock-electric experiments of hydrate-bearing sediments, both temperature and formation water salinity change, causing variations in the resistivity of the fully saturated formation water, as shown in Figure 2.

Figure 4 shows the relationship between the resistivity increase ratio RI and water saturation S_w. The blue line represents the $RI - S_w$ curve using R_{01} as the reference resistivity, while the red line represents the $RI - S_w$ curve using R_{02} as the reference resistivity. The curve fitting results indicate that the saturation exponent $n = 0.95$ for the R_{02} curve, which is significantly lower than the empirical value for water-wet sandstone reservoirs ($n = 2$).

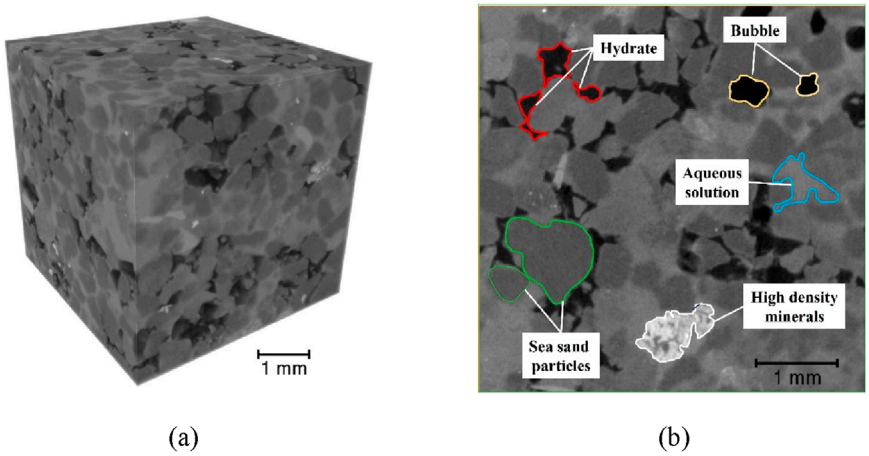

FIGURE 3
X-CT device and hydrate gray scale image: **(a)** shows the 3D grayscale image of hydrate; **(b)** shows the 2D gray profile of hydrate.

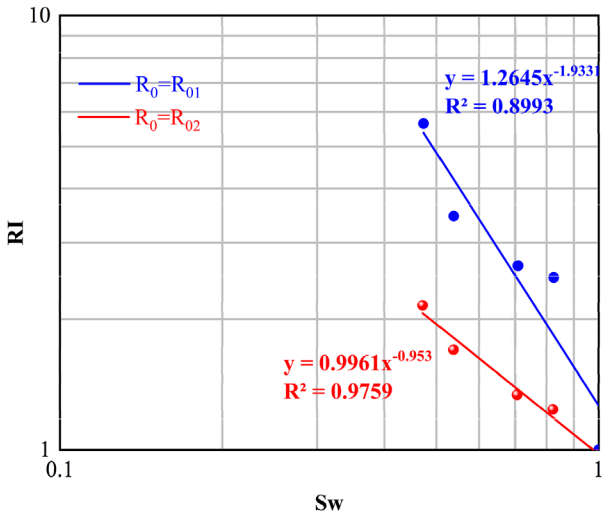

FIGURE 4
The $RI - S_w$ curve with different R_0.

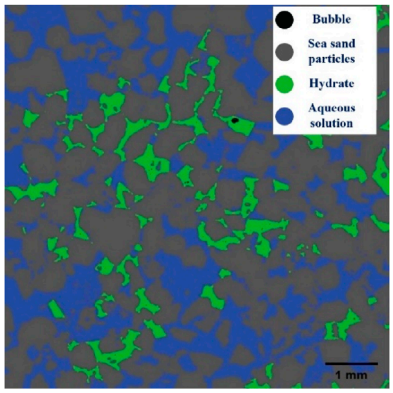

FIGURE 5
THF hydrate threshold segmentation images.

3.2 Spatial distribution characteristics of hydrates

The resistivity increase ratio of hydrate-bearing sediments depends not only on hydrate saturation but also on the spatial distribution of hydrates. Based on the *in-situ* CT scanning images during the hydrate formation process and subsequent digital image processing, the distribution patterns of hydrates within the pore space can be analyzed, as shown in Figure 5, the gray areas represent sea sand grains, the light green areas represent hydrates, the blue areas represent aqueous solutions, and the black areas represent bubbles.

Since THF is completely miscible with water, the mixed solution is uniformly distributed within the pores prior to hydrate formation. X-CT scanning was conducted to observe the saturation state, ensuring that all pores were nearly fully saturated. Using threshold segmentation, we extracted the pore space before hydrate formation and the THF hydrate phase at different time points, enabling the calculation of hydrate saturation over time. Further, the quantitative relationship between pore fluid resistivity and hydrate saturation is established. While this relationship may vary with different experimental conditions, the methodology for its determination remains universally applicable.

After quantitatively analyzing the spatial distribution of hydrates at different saturation levels, it was found that during the initial stage of hydrate formation, hydrates form in the center of the pores and are distributed in a dispersed manner. If a gas-liquid interface exists within the pore, hydrates preferentially form at this interface, with gas still occupying the central part of the pore. As the hydrate content increases, the distribution of hydrates gradually transitions from a dispersed to a suspended state, while the aqueous phase remains interconnected. As the hydrate content increases, the distribution gradually transitions from a dispersed to a suspended state, with the water phase maintaining connectivity. Within the pore network, this

continuous water phase forms a complete conductive path, leading to a slow increase in the resistivity index.

The distribution patterns of THF hydrates in the pore space are similar to the distribution of oil phases in the pores of pure water-wet samples in conventional oil and gas reservoirs. Since hydrates and oil phases exhibit similar resistivity characteristics, it can be inferred that the rock-electrical properties of sediments containing THF hydrates are expected to follow the Archie model (Archie, 1942).

4 Factors affecting the resistivity of sediments containing THF hydrates

Compared with the rock-electrical experiments on pure sandstone samples, the most significant differences in the rock-electrical experiments on hydrate-bearing sediments are as follows: (1) During hydrate formation, the salting-out effect increases the salinity of the formation water, altering its resistivity. This effect also inhibits hydrate formation, resulting in discrepancies between the actual hydrate saturation in the sediment pores and the theoretical saturation calculated based on mass ratios (Lu et al., 2019) (2) In hydrate formation experiments, the temperature decrease also affects the electrical conductivity of the formation water.

4.1 Influence of salting-out effect on the resistivity of hydrate-bearing sediments

In-situ CT scanning during hydrate formation provides a novel method for quantitatively characterizing the salting-out effect in formation water. As THF hydrates form, the salinity of the formation water increases, leading to a higher concentration of iodide ions per unit volume of formation water solution. This enhances the X-ray absorption coefficient of the formation water solution. According to the principles of CT imaging, the grayscale values of the formation water regions in the images increase with the salting-out effect.

Figures 6a–c show the two-dimensional grayscale images from CT scans at different stages of hydrate formation, with hydrate saturations of 0%, 13%, and 23%, respectively. The images were processed using image calibration and grayscale correction to ensure consistent grayscale values for quartz grains across all three images. This facilitates a quantitative comparison of grayscale changes at the same locations. The average grayscale values of the formation water solution at different hydrate saturations were analyzed, and the results are shown in Figure 7. The scanning results indicate that as the hydrate saturation increases, the brightness of the formation water solution regions gradually increases, demonstrating an elevated iodide ion concentration and confirming the salting-out effect during hydrate formation.

Sodium iodide (NaI) solutions with weight fractions of 7.3%, 8.1%, 12.5%, and 25% were prepared, and their resistivities were measured. The salinity of the formation water increases, the ionic conductivity of the formation water also enhances. Therefore, the formation water resistivity R_w in Equation 2 should correspond to the salinity of the formation water when the hydrate is fully formed.

Additionally, the THF hydrate lattice is a cage-like structure formed by water molecules through hydrogen bonds. Its cavities are sized and shaped to accommodate guest molecules that match both volume and geometry. Salt ions, however, are unable to enter the lattice due to size and charge repulsion (Sloan and Koh, 2007). In low salinity environments, hydrates form rapidly, consuming a large number of water molecules, which increases the mineralization of formation water. As the salinity of the formation water increases, it hinders the formation of hydrates (Ismail and Koh, 2022), resulting in discrepancies between the hydrate saturation calculated from the concentration of the THF solution and the actual hydrate saturation. When the salt ion concentration exceeds its solubility in water, the dissolved salts precipitate as solids, resulting in the salting-out effect. Before the salting-out effect occurs, the ion concentration in the pore fluids continues to rise, with a large number of freely mobile ions present in the formation water, enhancing the fluid's electrical conductivity and lowering the resistivity of the pore fluids (Devarakonda et al., 1999). After the onset of the salting-out effect, the precipitated salt crystals (NaI) no longer participate in electrical conduction but instead occupy pore space, blocking pores and throats or attaching to mineral surfaces, which affects the connectivity of the pore structure. The increased tortuosity of the pores alters the original conductive pathways, forcing the electric current to take longer routes and thereby increasing the resistivity of the pore fluids. X-ray CT scanning provides a novel method for quantitatively calculating the saturation of fully formed hydrates. For example, using a formation water solution with a NaI mass fraction of 5%, THF mixtures with weight fractions of 6.35%, 8.33%, 12.12%, and 19.05% were added to prepare the formation water solutions. According to Equation 4, the theoretical hydrate saturations are 30%, 40%, 60%, and 100%, respectively. By monitoring the temperature and pressure curves as well as the resistivity curves during the hydrate formation process, and ensuring stable temperature and pressure conditions in the reactor, X-ray CT scanning was used to obtain three-dimensional grayscale images of the sediments. The actual hydrate saturation was calculated based on image processing. The results show a significant difference between the actual hydrate saturation in the sediment pores and the theoretical saturation, as shown in Table 1. The water saturation S_w in Equation 6 should be based on the results calculated from the CT scan images.

With an initial NaI concentration of 5% in the formation water solution, the concentration of NaI in the formation water after complete hydrate formation can be calculated for different weight fractions of THF solutions, as shown in Table 1.

In summary, the salting-out effect during hydrate formation not only leads to changes in the salinity of the formation water but also inhibits hydrate formation due to high salinity, resulting in differences between the actual and theoretical hydrate saturations. Corrections are necessary when calculating the formation factor and resistivity increase ratio to account for these effects.

4.2 Influence of temperature on the resistivity of hydrate-bearing sediments

Temperature plays a crucial role in determining the electrical properties of sediments. On one hand, it affects the solubility of charged ions, thereby altering the ion concentration in the pore fluid. On the other hand, it influences the migration rate of these ions (Du Frane et al., 2015). In a saturated pore solution, a

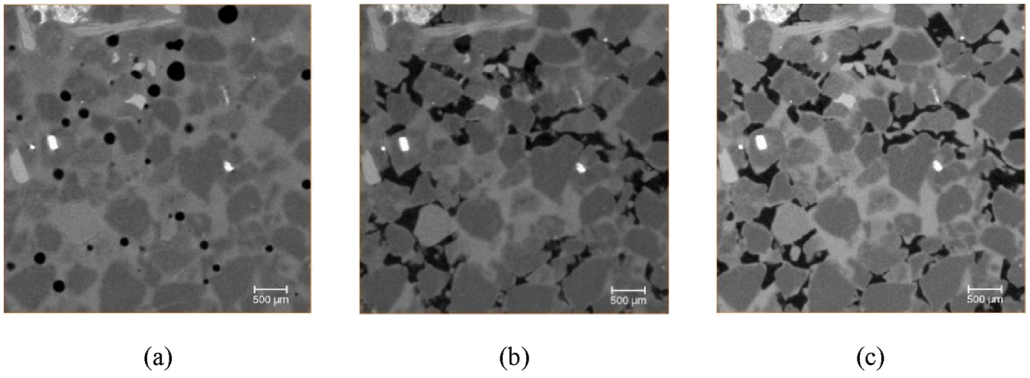

FIGURE 6
Scanning gray images of hydrate formation under different hydrate saturation states: **(a)** shows the Grayscale CT scan image of hydrate saturation at 0%; **(b)** shows the Grayscale CT scan image of hydrate saturation at 13%; **(c)** shows the Grayscale CT scan image of hydrate saturation at 23%.

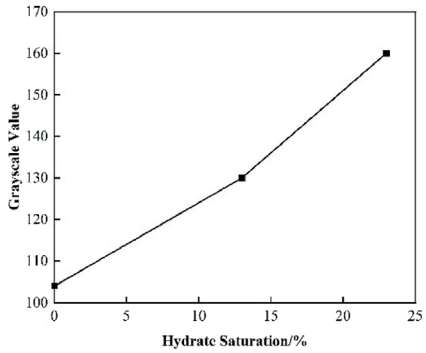

FIGURE 7
Relationship curve between solution gray value and hydrate saturation.

decrease in temperature induces solute precipitation, which reduces the concentration of charged ions and slows their migration rate, leading to a significant increase in pore fluid resistivity.

To quantitatively analyze the influence of temperature on the resistivity of formation water solutions, NaI solutions with different weight fractions were placed in the reactor, and the temperature was gradually lowered while the solution temperature and resistivity were recorded in real-time. The changes in resistivity of solutions with different NaI concentrations as a function of temperature are shown in Figure 8. At the same temperature, the resistivity decreases with increasing mass fraction of NaI; at the same mass fraction, the resistivity of the solution increases as the temperature decreases. The trend of resistivity changes with temperature for the 7.3% NaI solution, as shown in Figure 9, corresponds to the NaI concentration after complete hydrate formation from a 6.35% THF solution, as listed in Table 1.

Figure 10 shows the changes in temperature and resistivity during the formation of hydrates from a mixture with a THF concentration of 6.35% and a NaI concentration of 5%. The actual saturation of the formed hydrates is 30%, and the concentration of NaI in the solution is 7.3%. In Figure 9, when the temperature of the NaI solution decreases to 1°C, the increase in the resistivity of the formation water compared to room temperature is 69.5%. In Figure 10, when the temperature of the THF solution decreases over the same range, the increase in resistivity within the porous medium is 75.3%, which is close to the increase in resistivity of the formation water. This indicates that during the initial stage of temperature decrease (indicated by the dashed line range) in Figure 10, the increase in resistivity of the sediments is primarily due to the increase in resistivity of the formation water caused by the temperature drop. Therefore, the resistivity of the formation water used in the calculation of rock-electrical parameters for THF hydrate formation needs to be corrected for temperature.

4.3 Resistivity variation patterns after corrections for salting-out effect and temperature

Considering the influence of salting-out effect and temperature on the resistivity of hydrate-bearing sediments during THF hydrate formation, corrections are required for hydrate saturation, formation water temperature, and salinity.

(1) The final hydrate saturation corresponding to different THF concentrations was calculated based on CT scan images, with the results shown in Table 1.

(2) NaI solutions corresponding to the complete formation of hydrates from different THF concentrations were prepared, as shown in Table 1. These solutions were cooled to the temperature at which hydrates form, and the formation water resistivity R_w was measured at this temperature. For example, for a mixture with a THF concentration of 6.35% and a NaI concentration of 5%, the NaI concentration in the solution after complete hydrate formation is 7.3%. According to the experimental results, the resistivity of the 7.3% NaI solution varies with temperature, and the formation water resistivity is taken as $R_w = 0.336\ \Omega \cdot \mathrm{m}$.

(3) The cementation index m of the sediment model was measured to be 1.6. Given the formation water resistivity, the sediment resistivity R_0 at the saturation corresponding to the formation of hydrates can be obtained from Equation 2.

TABLE 1 Comparison of theoretical hydrate saturation and CT actual hydrate saturation.

No.	THF mass fraction/%	Theoretical saturation/%	CT actual saturation/%	The mass fraction of NaI after complete hydrate formation/%
1	6.35	30	18.11	7.3
2	8.33	40	29.46	8.1
3	12.12	60	46.37	12.5
4	19.05	100	52.78	25.0

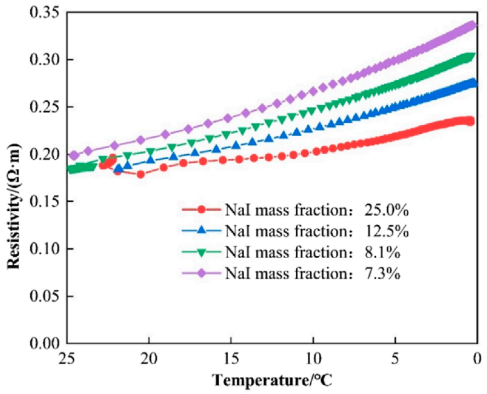

FIGURE 8
Dependence of NaI solution resistivity on temperature.

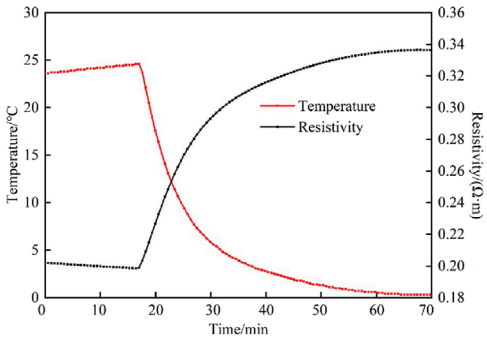

FIGURE 9
Resistivity and temperature curves of 7.3%NaI solution.

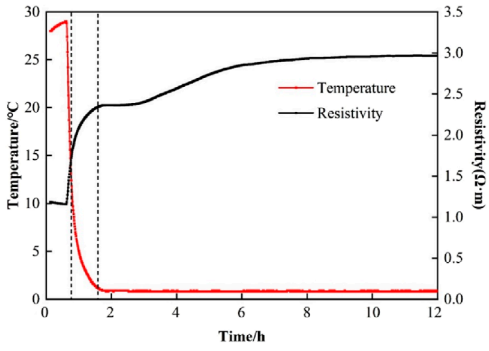

FIGURE 10
6.35%THF hydrate formation temperature and resistivity curve.

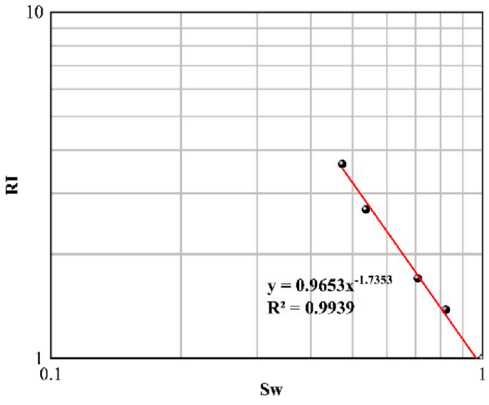

FIGURE 11
The corrected $RI - S_w$ curve of hydrate.

(4) The resistivity increase ratio was calculated using Equation 3, and the $RI - S_w$ curve was plotted. Curve fitting was used to determine the saturation exponent n.

After corrections for hydrate saturation, temperature, and formation water salinity, the relationship between water saturation and resistivity increase ratio for pure sandstone sediments is shown in Figure 11. The cementation index $m = 1.61$ and the saturation exponent $n = 1.73$ satisfy the Archie equation. Archie established a saturation exponent of approximately 2 based on electrical measurements of well-cemented, conventional water-wet sandstone reservoirs. In this study, considering the weak cementation of marine hydrate reservoirs, coarse sand was selected as the sediment medium. The larger pore size and better connectivity of the sediment, compared to strongly cemented and compacted oil and gas reservoirs, resulted in a lower saturation exponent.

5 Conclusion

In this study, we conducted a systematic investigation into the electrical resistivity of THF hydrate-bearing sediments by integrating *in-situ* CT scanning with resistivity measurements, The spatial distribution patterns of hydrate in the pore space were visualized through 3-D grayscale images obtained *via* micro-CT scanning. A detailed analysis was performed on the variations of electrical resistivity as functions of hydrate saturation and temperature. Furthermore, we examined the influence of the salt-out effect on both hydrate saturation and sediment resistivity. A corrected methodology was developed to account for the combined impacts of temperature and salt-out effect.

(1) The spatial distribution of THF hydrates within sand sediments is similar to that of oil phases in water-wet sandstone reservoirs. THF hydrates predominantly form at gas-liquid interfaces, transitioning from a dispersed to a suspended state as saturation increases. This distribution significantly influences both the connectivity of the pore water phase and the sediment's overall resistivity.
(2) The salting-out effect during THF hydrate formation significantly increases the salinity of the formation water, thereby enhancing ionic conductivity and decreasing resistivity. This effect inhibits hydrate growth, resulting in actual hydrate saturations that are lower than theoretical predictions. The difference between actual and theoretical saturations becomes more pronounced at higher hydrate saturations.
(3) The electrical properties of sediments are critically affected by temperature. Lower temperatures lead to higher resistivity in formation water, resulting from decreased ion mobility and solubility.
(4) After accounting for salting-out effects and temperature variations, the relationship between water saturation and resistivity index agrees well with Archie's equations, with a cementation index of 1.61 and a saturation exponent of 1.73.

These findings enhance our understanding of THF hydrate formation in geological settings and provide valuable insights for optimizing oil and gas exploration and development strategies. It is important to note that the current model is based on laboratory conditions and may not fully account for the complexities of natural geological environments. Further studies are needed to validate these findings under field conditions.

Data availability statement

The raw data supporting the conclusions of this article will be made available by the authors, without undue reservation.

Author contributions

FeX: Conceptualization, Formal Analysis, Validation, Writing–original draft. MC: Data curation, Investigation, Writing–review and editing. ML: Data curation, Validation, Writing–review and editing. QD: Writing–review and editing. FuX: Writing–review and editing. ZL: Writing–review and editing. JH: Writing–review and editing. XL: Funding acquisition, Project administration, Writing–review and editing.

Funding

The author(s) declare that financial support was received for the research, authorship, and/or publication of this article. To accomplish this work, the authors would like to gratefully acknowledge the supported by the National Nature Science Foundation of China (No. 42274158) and National Nature Science Foundation of China (No. 52334002).

Acknowledgments

We thank China University of Petroleum (East) and CNOOC (China National Offshore Oil Corporation) for permission to publish this work. Opinions presented in this paper represent only the author's personal viewpoints. Contributions from Qin Dai and Xuefeng Liu are greatly acknowledged.

Conflict of interest

Author MC was employed by CNOOC(China) Co, Ltd.

The remaining authors declare that the research was conducted in the absence of any commercial or financial relationships that could be construed as a potential conflict of interest.

Generative AI statement

The author(s) declare that no Generative AI was used in the creation of this manuscript.

Publisher's note

All claims expressed in this article are solely those of the authors and do not necessarily represent those of their affiliated organizations, or those of the publisher, the editors and the reviewers. Any product that may be evaluated in this article, or claim that may be made by its manufacturer, is not guaranteed or endorsed by the publisher.

References

Archie, G. E. (1942). The electrical resistivity log as an aid in determining some reservoir characteristics. *Trans. AIME* 146 (01), 54–62. doi:10.2118/942054-g

Asadi, F., Ejtemaei, M., Birkett, G., Searles, D. J., and Nguyen, A. V. (2019). The link between the kinetics of gas hydrate formation and surface ion distribution in the low salt concentration regime. *Fuel* 240, 309–316. doi:10.1016/j.fuel.2018.11.146

Chen, Q., Wu, N., Liu, C., Zou, C., Liu, Y., Sun, J., et al. (2022). Research progress on global marine gas hydrate resistivity logging and electrical property experiments. *J. Mar. Sci. Eng.* 10 (5), 645. doi:10.3390/jmse10050645

Chen, Y., Wu, N., Liang, D., and Hu, R. (2018). Numerical simulation on the resistivity of hydrate-bearing sediment based on the fractal pore model. *Nat. Gas. Ind.* 38 (11), 128–134. doi:10.3787/j.issn.1000-0976.2018.11.017

Chong, Z. R., Yang, S. H. B., Babu, P., Linga, P., and Li, X.-S. (2016). Review of natural gas hydrates as an energy resource: prospects and challenges. *Appl. Energy* 162, 1633–1652. doi:10.1016/j.apenergy.2014.12.061

Collett, T. S., and Lee, M. W. (2012). Well log characterization of natural gas-hydrates. *Petrophysics* 53 (05), 348–367.

Devarakonda, S., Groysman, A., and Myerson, A. S. (1999). THF–water hydrate crystallization: an experimental investigation. *J. Cryst. Growth* 204 (4), 525–538. doi:10.1016/S0022-0248(99)00220-1

Dong, H., Sun, J., Zhu, J., Liu, L., Lin, Z., Golsanami, N., et al. (2019). Developing a new hydrate saturation calculation model for hydrate-bearing sediments. *Fuel* 248, 27–37. doi:10.1016/j.fuel.2019.03.038

Du, K., Xi, W., Huang, S., and Zhou, J. (2024). Deep-sea mineral resource mining: a historical review, developmental progress, and insights. *Min. Metallurgy and Explor.* 41 (1), 173–192. doi:10.1007/s42461-023-00909-9

Du Frane, W. L., Stern, L. A., Constable, S., Weitemeyer, K. A., Smith, M. M., and Roberts, J. J. (2015). Electrical properties of methane hydrate+ sediment mixtures. *J. Geophys. Res. solid earth* 120 (7), 4773–4783. doi:10.1002/2015JB011940

Fang, B., Ning, F., Cao, P., Peng, L., Wu, J., Zhang, Z., et al. (2017). Modeling thermodynamic properties of propane or tetrahydrofuran mixed with carbon dioxide or methane in structure-II clathrate hydrates. *J. Phys. Chem. C* 121 (43), 23911–23925. doi:10.1021/acs.jpcc.7b06623

Guerin, G., Goldberg, D., and Meltser, A. (1999). Characterization of *in situ* elastic properties of gas hydrate-bearing sediments on the Blake Ridge. *J. Geophys. Res. Solid Earth* 104 (B8), 17781–17795. doi:10.1029/1999JB900127

Hassanpouryouzband, A., Joonaki, E., Vasheghani Farahani, M., Takeya, S., Ruppel, C., Yang, J., et al. (2020). Gas hydrates in sustainable chemistry. *Chem. Soc. Rev.* 49 (15), 5225–5309. doi:10.1039/C8CS00989A

Hirai, H., Uchihara, Y., Fujihisa, H., Sakashita, M., Katoh, E., Aoki, K., et al. (2001). High-pressure structures of methane hydrate observed up to 8 GPa at room temperature. *J. Chem. Phys.* 115 (15), 7066–7070. doi:10.1063/1.1403690

Ismail, N. A., and Koh, C. A. (2022). Growth rate and morphology study of tetrahydrofuran hydrate single crystals and the effect of salt. *CrystEngComm* 24 (23), 4301–4311. doi:10.1039/D2CE00176D

Jin, Y., Li, S., and Yang, D. (2020). Experimental and theoretical quantification of the relationship between electrical resistivity and hydrate saturation in porous media. *Fuel* 269, 117378. doi:10.1016/j.fuel.2020.117378

Kalender, W. A. (2006). X-ray computed tomography. *Phys. Med. and Biol.* 51 (13), R29–R43. doi:10.1088/0031-9155/51/13/R03

Konno, Y., Masuda, Y., Akamine, K., Naiki, M., and Nagao, J. (2016). Sustainable gas production from methane hydrate reservoirs by the cyclic depressurization method. *Energy Convers. Manag.* 108, 439–445. doi:10.1016/j.enconman.2015.11.030

Lee, J. Y., Yun, T. S., Santamarina, J. C., and Ruppel, C. (2007). Observations related to tetrahydrofuran and methane hydrates for laboratory studies of hydrate-bearing sediments. *Geochem. Geophys. Geosystems* 8 (6). doi:10.1029/2006GC001531

Li, B., Nie, X., Cai, J., Zhou, X., Wang, C., and Han, D. (2022a). U-Net model for multi-component digital rock modeling of shales based on CT and QEMSCAN images. *J. Petroleum Sci. Eng.* 216, 110734. doi:10.1016/j.petrol.2022.110734

Li, F., Sun, C., Li, S., Chen, G., Guo, X., Yang, L., et al. (2012). Experimental studies on the evolvement of electrical resistivity during methane hydrate formation in sediments. *Energy and Fuels* 26 (10), 6210–6217. doi:10.1021/ef301257z

Li, H., Liu, J., Qu, C., Song, H., and Zhuang, X. (2022b). A method for calculating gas hydrate saturation by dual parameters of logging. *Front. Earth Sci.* 10. doi:10.3389/feart.2022.986647

Li, X., Li, B., Liu, F., Li, T., and Nie, X. (2023). Advances in the application of deep learning methods to digital rock technology. *Adv. Geo-Energy Res.* 8 (1), 5–18. doi:10.46690/ager.2023.04.02

Li, Y., Sun, H., Meng, Q., Liu, C., Chen, Q., and Xing, L. (2020). 2-D electrical resistivity tomography assessment of hydrate formation in sandy sediments. *Nat. Gas. Ind. B* 7 (3), 278–284. doi:10.1016/j.ngib.2019.10.010

Li, Z., Xia, Z., Chen, Z., Li, X., Xu, C., and Yan, R. (2019). The plateau effects and crystal transition study in Tetrahydrofuran (THF)/CO2/H2 hydrate formation processes. *Appl. Energy* 238, 195–201. doi:10.1016/j.apenergy.2018.12.080

Lijith, K. P., Malagar, B. R. C., and Singh, D. N. (2019). A comprehensive review on the geomechanical properties of gas hydrate bearing sediments. *Mar. Petroleum Geol.* 104, 270–285. doi:10.1016/j.marpetgeo.2019.03.024

Lu, R., Stern, L. A., Du Frane, W. L., Pinkston, J. C., Roberts, J., and Constable, S. (2019). The effect of brine on the electrical properties of methane hydrate. *J. Geophys. Res. Solid Earth* 124 (11), 10877–10892. doi:10.1029/2019JB018364

Nagashima, K., Orihashi, S., Yamamoto, Y., and Takahashi, M. (2005). Encapsulation of saline solution by tetrahydrofuran clathrate hydrates and inclusion migration by recrystallization. *J. Phys. Chem. B* 109 (20), 10147–10153. doi:10.1021/jp040680i

Pearson, C., Murphy, J., and Hermes, R. (1986). Acoustic and resistivity measurements on rock samples containing tetrahydrofuran hydrates: laboratory analogues to natural gas hydrate deposits. *J. Geophys. Res. Solid Earth* 91 (B14), 14132–14138. doi:10.1029/JB091iB14p14132

Ren, S. R., Liu, Y., Liu, Y., and Zhang, W. (2010). Acoustic velocity and electrical resistance of hydrate bearing sediments. *J. Petroleum Sci. Eng.* 70 (1), 52–56. doi:10.1016/j.petrol.2009.09.001

Sahu, C., Kumar, R., and Sangwai, J. S. (2020). Comprehensive review on exploration and drilling techniques for natural gas hydrate reservoirs. *Energy and Fuels* 34 (10), 11813–11839. doi:10.1021/acs.energyfuels.0c02202

Shankar, U., and Riedel, M. (2011). Gas hydrate saturation in the Krishna–Godavari basin from P-wave velocity and electrical resistivity logs. *Mar. Petroleum Geol.* 28 (10), 1768–1778. doi:10.1016/j.marpetgeo.2010.09.008

Sloan, E. D., and Koh, C. A. (2007). *Clathrate hydrates of natural gases*. 3rd ed. Boca Paton: CRC Press.

Spangenberg, E., and Kulenkampff, J. (2006). Influence of methane hydrate content on electrical sediment properties. *Geophys. Res. Lett.* 33 (24). doi:10.1029/2006GL028188

Tan, Z., Pan, G., and Liu, P. (2016). Focus on the development of natural gas hydrate in China. *Sustainability* 8 (6), 520. doi:10.3390/su8060520

Wang, X., Wu, S., Lee, M., Guo, Y., Yang, S., Liang, J. J. M., et al. (2011). Gas hydrate saturation from acoustic impedance and resistivity logs in the Shenhu area, South China Sea. *Mar. Petroleum Geol.* 28 (9), 1625–1633. doi:10.1016/j.marpetgeo.2011.07.002

Wei, N., Pei, J., Zhao, J., Zhang, L., Zhou, S., Luo, P., et al. (2022). A state-of-the-art review and prospect of gas hydrate reservoir drilling techniques. *Front. Earth Sci.* 10. doi:10.3389/feart.2022.997337

Wilcox, W. I., Carson, D. B., and Katz, D. L. (1941). Natural gas hydrates. *Industrial and Eng. Chem.* 33 (5), 662–665. doi:10.1021/ie50377a027

Xing, L., Niu, J., Zhang, S., Cao, S., Wang, B., Lao, L., et al. (2022). Experimental study on hydrate saturation evaluation based on complex electrical conductivity of porous media. *J. Petroleum Sci. Eng.* 208, 109539. doi:10.1016/j.petrol.2021.109539

Yang, M., Song, Y., Liu, Y., Lam, W.-H., Li, Q., and Yu, X. (2012). Effects of halogen ions on phase equilibrium of methane hydrate in porous media. *Int. J. Thermophys.* 33 (5), 821–830. doi:10.1007/s10765-012-1191-3

Yu, Y.-S., Zhang, X., Liu, J.-W., Lee, Y., and Li, X.-S. (2021). Natural gas hydrate resources and hydrate technologies: a review and analysis of the associated energy and global warming challenges. *Energy and Environ. Sci.* 14 (11), 5611–5668. doi:10.1039/D1EE02093E

Yun, T. S., Santamarina, J. C., and Ruppel, C. (2007). Mechanical properties of sand, silt, and clay containing tetrahydrofuran hydrate. *J. Geophys. Res. Solid Earth* 112 (B4). doi:10.1029/2006jb004484

Zhang, Z., Liu, L., Li, C., Cai, J., Ning, F., Meng, Q., et al. (2021). Fractal analyses on saturation exponent in Archie's law for electrical properties of hydrate-bearing porous media. *J. Petroleum Sci. Eng.* 196, 107642. doi:10.1016/j.petrol.2020.107642

Zhou, S., Li, Q., Lv, X., Pang, W., and Fu, Q. (2019). Thinking and suggestions on research direction of natural gas hydrate development. *China Offshore Oil Gas.* 31 (4), 1–8. doi:10.11935/j.issn.1673-1506.2019.04.001